JOURNAL OF FUEL CHEMISTRY AND TECHNOLOGY
Volume 54, Issue 7, July 2026

燃料化学学报(中英文)
Journal of Fuel Chemistry and Technology

Cite this article as: J Fuel Chem Technol, 2026, 54, 20250277

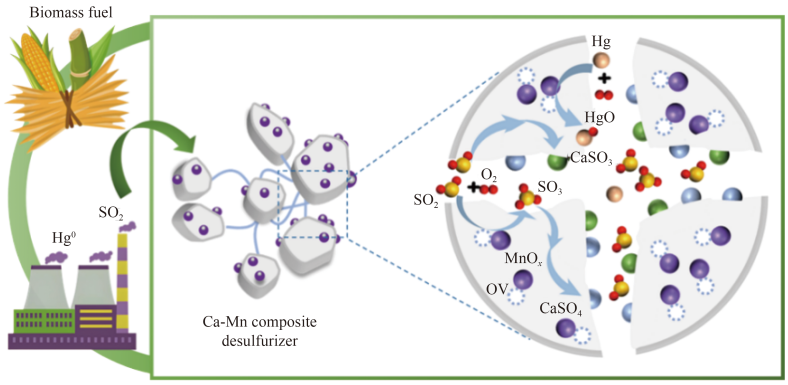
RESEARCH PAPER

Construction of calcium-manganese composite desulfurizer for synergistic removal of SO_2/Hg^0

LIU Shuaipeng[1,2], LI Dalai[1,2], REN Zihan[1,2], LIU Jie[1,2,*], WANG Lidong[1,2]

[1] Yanzhao Electric Power Laboratory of North China Electric Power University, Baoding 071003, China;
[2] Department of Environmental Science and Engineering, North China Electric Power University, Baoding 071003, China

Abstract: Under the carbon neutrality strategy, biomass boilers have emerged as key facilities for renewable energy utilization, yet are characterized by low-concentration SO_2 emissions. Ca-based dry desulfurization presents a promising technology for biomass boiler flue gas purification due to its compact structure, low capital investment and simple operation and maintenance. However, it is generally limited by the low adsorbent utilization and insufficient desulfurization efficiency. Herein, this study developed a novel Ca-Mn composite adsorbent through a synergistic strategy integrating F127 surfactant to optimize dispersion and Mn loading to enhance oxidation efficiency. The resulting adsorbent not only significantly increased the breakthrough sulfur capacity of the Ca-based material but also markedly improved the synergistic removal of Hg^0. It was demonstrated that the introduction of Mn elements and F127 effectively suppressed the agglomeration of $Ca(OH)_2$ crystallites and induced an oxygen vacancy-rich structure, while simultaneously optimizing the pore structure of the adsorbent. The modified adsorbent exhibited the enlarged specific surface area and pore volume, which favored to enhance the reaction mass transfer and effectively prevent the pore blockage and coverage of active sites by desulfurization products. The Mn sites and oxygen vacancies formed catalytic centers, which not only accelerated the desulfurization reaction by promoting SO_2 oxidation but also enabled the adsorbent to couple with Hg^0 catalytic oxidation functionality. Consequently, the simultaneous removal of SO_2 and Hg^0 was significantly enhanced on the Ca-Mn composite adsorbent.



Key words: calcium-manganese composite; oxygen vacancy; dry desulfurization; Hg^0; synergistic control

Biomass boilers, as a key medium for biomass energy utilization, are emerging as pivotal supporting technologies for the global energy transition, offering substantial advantages such as low operating costs, high thermal efficiency, waste-to-resource conversion, and zero-carbon emission. From the perspective of flue gas pollutant control, the SO_2 emission concentration from biomass boilers is typically below 300 mg/m^3, classifying it as low-sulfur flue gas[1−2]. For low-concentration SO_2, dry desulfurization technology utilizing Ca-based adsorbents offers distinct advantages, including a compact system design, low investment costs, and ease of operation and maintenance, thus enhancing its potential competitiveness in the biomass boiler flue gas purification field[3−4]. However, with the increasing stringency of national environmental standards, both the desulfurization efficiency of dry processes and the utilization rate of Ca-based adsorbents require further enhancement. The development of novel Ca-based materials with high specific surface areas and controllable pore structures has become a key breakthrough for enhancing the overall performance of dry desulfurization[5−6].

Studies have demonstrated that the inadequate

Received: 2025-10-11; Revised: 2025-12-01
Foundation items: Supported by National Key R&D Program of China (2022YFC3701600) and National Nature Science Foundation of China (52270103).
* Corresponding author. Tel: 0312-7525515, E-mail: jie.liu@ncepu.edu.cn.
DOI: 10.1016/S1872-5813(26)60656-1 CSTR: 32157.14.2097-213X.2026.JFCT.0011 Associated Data DOI: 10.57760/sciencedb.33124
本文的英文电子版由 Elsevier 出版社在 ScienceDirect 上出版 (http://www.sciencedirect.com/science/journal/18725813)

desulfurization performance of Ca-based materials, particularly $Ca(OH)_2$, is mainly due to: (1) the low intrinsic reactivity between $Ca(OH)_2$ and SO_2; and (2) the formation of dense $CaSO_3$/$CaSO_4$ layers on the material surface during desulfurization, which would block the reaction channels and severely hinder the mass transfer[7−8]. To address these limitations, the modification by functional additives has emerged as a key strategy to modulate the physicochemical properties of Ca-based adsorbents and enhance their performance. For instance, Xing et al.[9] developed a $Ca(OH)_2$/Al_2O_3 composite adsorbent in which the synergistic effect of high-specific-surface-area Al_2O_3 and organic surfactants substantially improved the dispersion of active Ca-based components, thereby increasing the gas-solid reaction interface area and significantly boosting desulfurization efficiency. Fan et al.[10] and Yu et al.[11] found that the introduction of surfactants (e.g., sodium dodecyl sulfate, ethanol, and diethylene glycol) could significantly reduce the hydration rate of CaO, which facilitated the formation of $Ca(OH)_2$ materials with a larger specific surface area, and consequently enhanced the saturated sulfur capacity. Furthermore, optimizing the reaction pathway of SO_2 provides an effective method to improve the desulfurization performance of calcium-based materials. Using a catalytic oxidation pre-treatment strategy, converting SO_2 to the more reactive SO_3 can substantially lower the desulfurization reaction energy barrier and increase the reaction rate. Zhong et al.[12] modified an industrial-grade $Ca(OH)_2$ adsorbent by the co-loading of Fe_2O_3/MgO. Attributed to the synergistic effect of Fe_2O_3 catalysis and MgO alkaline absorption, the modified Ca-based material demonstrated markedly superior desulfurization performance compared to commercially available $Ca(OH)_2$. Yao et al.[13] developed a Mn/Ce modified $Ca(OH)_2$ adsorbent. They observed that the Mn/Ce co-doping induced the formation of abundant oxygen vacancies within the structure of the Ca-based material, thereby enhancing its reactivity with SO_2. Similarly, Wang et al.[14] investigated the effects of MnO_2, Fe_2O_3 and CeO_2 in promoting the desulfurization performance of Ca-based materials, and identified MnO_2 as the most effective catalyst among them.

In addition to the low-concentration SO_2 emissions, flue gas from biomass boilers tends to enrich trace heavy metal components, such as Hg, As, Pb, Cd and Cr. Among them, mercury pollutants have become a key regulated substance in the international environmental field due to their unique environmental behaviors, such as high toxicity, bioaccumulation potential, and long-range transport capacity[15−16]. Mercury in flue gas exists in three forms: particulate-bound mercury (Hg^P), oxidized mercury (Hg^{2+}), and elemental mercury (Hg^0). Hg^P and Hg^{2+} can be effectively removed through dust removal and wet flue gas desulfurization systems, respectively. Hg^0 generally constitutes the largest fraction of mercury in flue gas and possesses characteristics of high volatility and low water solubility. Though partial Hg^0 can be adsorbed onto the surface of fly ash and captured by the dust removal system, or converted into Hg^{2+} *via* selective catalytic reduction of NO_x, its removal efficiency within the flue gas pollution control system generally remains low, thus limiting the overall efficiency of mercury control in flue gas systems[17−18]. Therefore, the development of novel Ca-based adsorbents for the co-removal of SO_2 and Hg^0 is of great industrial application value. However, current research on Ca-based adsorbents mainly centers on the pore structure modulation and catalytic site incorporation for enhancing desulfurization, with little consideration given to their potential for Hg^0 co-removal and the corresponding structural control.

Based on this, this study developed a novel Ca-Mn composite adsorbent. By introducing Mn species, abundant oxygen vacancies (OVs) were constructed and acted as the active sites for catalytic oxidation of SO_2 and Hg^0 in conjunction with the Mn sites. Meanwhile, the surfactant F127 was employed as the modifier to enhance the dispersion of Mn sites and suppress the agglomeration of Ca-based material grains, thereby optimizing the pores structure of material and the distribution of surface active sites. Based on the typical operating conditions of medium-temperature dry desulfurization systems in biomass boilers (temperature above 300 °C, relative humidity 10%−30%, NO_x concentration of $(2.0−6.0)\times10^{-4}$, and O_2 concentration of 4%), the simultaneous SO_2/Hg^0 removal performance of the Ca-Mn composite adsorbent and its adaptability to varying flue gas conditions were studied. Furthermore, combining characterization techniques such as X-ray diffraction (XRD), X-ray photoelectron spectroscopy (XPS), N_2 adsorption-desorption, and electron spin resonance (ESR), the promoting effects of the synergistic modification *via* Mn doping and surfactant protection on reaction mass transfer and SO_2/Hg^0 oxidation were revealed, and the synergistic pathway between the absorption of SO_2 and the catalytic oxidation of Hg^0 was elucidated. This study provides a new approach for the design and preparation of multifunctional Ca-based adsorbents, providing a theoretical foundation and technical insights for the development of dry cooperative control technologies targeting multi-pollutants in biomass boiler flue gas.

1 Materials and methods

1.1 Materials

Calcium chloride ($CaCl_2$, analytical grade), sodium hydroxide (NaOH, analytical grade), 50% manganese nitrate solution ($Mn(NO_3)_2$, analytical grade), calcium lignosulfonate ($C_{20}H_{24}CaO_{10}S_2$, analytical grade), Pluronic F127 (average molecular weight 13000, analytical grade), and absolute ethanol (C_2H_5OH, analytical grade) were purchased from Shanghai Macklin Biochemical Technology

Co., Ltd. The water used in the experiments was deionized (DI) water with the resistivity of 16 MΩ/cm.

1.2 Adsorbent preparation

Preparation of Mn-modified Ca-based adsorbent: 8.88 g of $CaCl_2$, 3.2 g of NaOH, varying amounts of F127 (0, 0.1, 0.2, 0.3 g), and volumes of $Mn(NO_3)_2$ solution (0, 40, 45, 50 μL) were mixed into 70 mL of DI water. The mixture was stirred continuously at room temperature for 30 min. The resultant product was washed with DI water and absolute ethanol until neutral pH was reached, and then dried in an oven at 60 °C for 12 h. Subsequently, the mixture was calcined in a muffle furnace at 500 °C for 4 h, with the heating rate of 10 °C/min, to obtain the precursor of the modified Ca-based adsorbent. Next, 1.5 g of the modified Ca-based adsorbent precursor and 0.03 g of $C_{20}H_{24}CaO_{10}S_2$ were mixed into 70 mL of DI water and stirred at room temperature for 30 min. The mixture was then transferred into a 100 mL reactor and reacted at 120 °C for 3 h. The final product was washed three times with DI water and absolute ethanol, then dried in an oven at 60 °C for 12 h to obtain the Mn-modified Ca-based adsorbent. The Mn-modified Ca-based adsorbents are labeled as Mn-*x*/F-*y*, where *x* represents the volume of $Mn(NO_3)_2$ solution used (*x* = 40, 45, 50 μL) and *y* represents the mass of F127 used (*y* = 0.1, 0.2, 0.3 g).

As controls, the following adsorbents were prepared: an unmodified Ca-based adsorbent without F127 surfactant or Mn doping, using a method similar to that of the Mn-modified version but without the addition of F127 and $Mn(NO_3)_2$ solution, labeled as $Ca(OH)_2$; a Ca-based adsorbent modified solely with F127 surfactant, prepared similarly but without $Mn(NO_3)_2$, labeled as $Ca(OH)_2$/F-*y* (where *y* denotes the usage of F127); and a Ca-based adsorbent modified solely with Mn, prepared similarly but without F127, labeled as Mn-*x* (where *x* denotes the volume of $Mn(NO_3)_2$ solution used).

1.3 Adsorbent characterizations

The Mn content in the modified Ca-based adsorbents was quantified using inductively coupled plasma optical emission spectrometry (ICP-OES, AGILENT 730). The morphology of the Ca-based adsorbents was analyzed using scanning electron microscopy (SEM, HITACHI SU8010) and transmission electron microscopy (TEM, FEI-Talos F200S). The phase structure of the samples was characterized using X-ray diffraction (XRD, Bruker D8 Advance). The surface chemical properties were examined using X-ray photoelectron spectroscopy (XPS, Thermo Fisher K-Alpha). N_2 adsorption-desorption tests were conducted using a specific surface area and porosity analyzer (Autosorb-iQ, American Konta) to investigate the physical properties of the samples. The defect structures were characterized using low-temperature electron paramagnetic resonance (ESR, Bruker A300).

1.4 Desulfurization and mercury removal performance evaluation

The desulfurization performance of the as-prepared adsorbents was assessed using a fixed-bed reactor. The adsorbent dosage was 0.3 g (0.25–0.38 mm), the inner diameter of the quartz tube reactor was 8 mm, and the simulated flue gas consisted of 4.0×10^{-4} SO_2, 4% O_2, with N_2 as the balance gas. The total flow rate of the simulated flue gas was 1000 mL/min, corresponding to a gas hourly space velocity (GHSV) of 26000 h^{-1}. The SO_2 concentrations at the inlet and outlet of the fixed-bed reactor were measured using a multi-component flue gas analyzer (ECOM-J2KN, Germany). The desulfurization performance was evaluated by the SO_2 removal efficiency (η_{SO_2}, %) and breakthrough sulfur capacity (*S*, mg/g), calculated using Equations (1) and (2), respectively. The desulfurization efficiency of 70% was established as the critical threshold, the corresponding outlet SO_2 concentration was defined as the breakthrough concentration, and the time required to reach this concentration was recorded as the breakthrough time.

$$\eta_{SO_2} = \frac{C_{0,1} - C_{i,1}}{C_{0,1}} \times 100\% \quad (1)$$

$$S = \left[\sum_{i=0}^{n} (C_{0,1} - C_{i,1}) \times t_i\right] \times \frac{Q}{m} \quad (2)$$

where $C_{0,1}$ $C_{i,1}$ represent the SO_2 concentrations at the inlet and outlet of the fixed-bed, respectively (mg/m^3), t_i is the data recording interval (2 min), Q is the flow rate of the simulated flue gas (m^3/min) and m is the mass of the adsorbent (g).

During the mercury removal performance tests, the elemental mercury (Hg^0) concentration was 70 μg/m^3, the O_2 concentration was 4%, the SO_2 concentration ranged from 0 to 4.0×10^{-4} (when used), and the NO concentration ranged from 0 to 6.0×10^{-4} (when used), with N_2 as the balance gas. The total flue gas flow rate was 1000 mL/min, corresponding to a gas hourly space velocity (GHSV) of 26000 h^{-1}. A Lumex RA-915+ mercury analyzer was employed for real-time monitoring of the Hg^0 concentration. The mercury removal capability was evaluated using the Hg^0 removal efficiency (η_{Hg^0}, %), calculated according to Equation (3).

$$\eta_{Hg^0} = \frac{C_{0,2} - C_{i,2}}{C_{0,2}} \times 100\% \quad (3)$$

where $C_{0,2}$ and $C_{i,2}$ are the Hg^0 concentrations (μg/m^3) at the inlet and outlet, respectively.

2 Results and discussion

2.1 Characterization of adsorbent properties

2.1.1 Crystal structure of adsorbents

The concentration of Mn element in the modified Ca-

based adsorbents was determined through ICP analysis. As presented in Table 1, the Mn contents in the Mn-40, Mn-45, Mn-50 and Mn-45/F-0.2 materials are 0.26%, 0.29%, 0.32% and 0.28%, respectively. The Mn concentration in the Mn-45 and Mn-45/F-0.2 samples are comparable. The crystal structure of the synthesized adsorbents was characterized using XRD. As depicted in Figure 1(a), the XRD pattern of the $Ca(OH)_2$ sample corresponds with the $Ca(OH)_2$ standard PDF card (PDF#01-076-0571), confirming the successful synthesis of a high-purity $Ca(OH)_2$ material. The diffraction peaks of the Mn-*x* adsorbents correspond to the characteristic crystal structure of $Ca(OH)_2$, with no diffraction signals of MnO_x phases detected, possibly due to the low concentration of Mn species. Meanwhile, with the increase of Mn doping, the intensity of the characteristic peaks of $Ca(OH)_2$ was decreased gradually, indicating that the incorporation of Mn resulted in lattice distortion of $Ca(OH)_2$, by substituting the Ca^{2+} sites or occupying the interstitial positions. Figure 1(b) compares the XRD patterns of the $Ca(OH)_2$, $Ca(OH)_2$/F-0.2, Mn-45 and Mn-45/F-0.2 adsorbents. The diffraction peaks of the $Ca(OH)_2$/F-0.2 and Mn-45/F-0.2 materials are consistent with the characteristic crystal structure of $Ca(OH)_2$. However, the introduction of Mn species and F127 template resulted in a significant decrease in the intensity of the characteristic peaks. The diffraction peak intensities of the adsorbents decreased by the order of $Ca(OH)_2$ > $Ca(OH)_2$/F-0.2 > Mn-45 > Mn-45/F-0.2. This indicates that both Mn doping and F127 introduction exhibit a significant synergistic effect in inhibiting crystal grain growth, with Mn doping exerting a stronger inhibitory effect than F127.

Table 1 Concentration of Mn element in various Mn-decorated Ca-based adsorbent

Adsorbent	Mn concentration *w*/%
Mn-40	0.26
Mn-45	0.29
Mn-50	0.32
Mn-45/F-0.2	0.28

2.1.2 Morphology of adsorbents

Figure 2 illustrates the SEM images of the Ca-based adsorbents. As depicted in Figure 2(a), the $Ca(OH)_2$ sample displays an irregular microstructure, consisting of a combination of nanoparticles and bulk structures, with particle sizes ranging approximately from 0.5 to 2 μm. Figure 2(b)–(d) show that both F127 surfactant modification and Mn doping effectively optimized the microstructure of the adsorbents, resulting in similar nanoparticle structures with a relatively uniform particle size of approximately 200–300 nm, although some particle agglomeration is still visible. Figure 2(d) displays the SEM image of the Mn-45/F-0.2 adsorbent. In contrast, the synergistic modification with the F127 surfactant and Mn doping led to a more regular microstructure of the adsorbent and effectively suppressed nanoparticle agglomeration, resulting in the Ca-based adsorbent with the promoted dispersion.

Figure 3 presents the TEM and HRTEM images of the prepared adsorbents. The TEM results further confirm the smaller particle sizes and enhanced dispersion of the Mn-45/F-0.2 adsorbent. In the HRTEM images, the lattice spacings of 0.121 and 0.114 nm correspond to the (113) and (104) planes of $Ca(OH)_2$, respectively. Due to the low Mn doping content, characteristic lattice spacings of MnO_x species were not observed in the Mn-45 and Mn-45/F-0.2 samples. Figure 3(e) presents the elemental mapping of the Mn-45/F-0.2 sample, demonstrating the uniform distribution of Mn within the Ca-based adsorbent.

2.1.3 Physical structure of adsorbents

The physical properties of adsorbents were investigated through N_2 adsorption-desorption analysis. As shown in Figure 4(a), the $Ca(OH)_2$, $Ca(OH)_2$/F-0.2, Mn-45 and Mn-45/F-0.2 samples exhibit typical type IV adsorption isotherms with H3-type hysteresis loops, indicating that the materials are mesoporous and feature slit-shaped pores with a non-uniform pore size distribution. Moreover, the Mn-doped adsorbents, Mn-45 and Mn-45/F-0.2, demonstrate higher N_2 adsorption capacities.

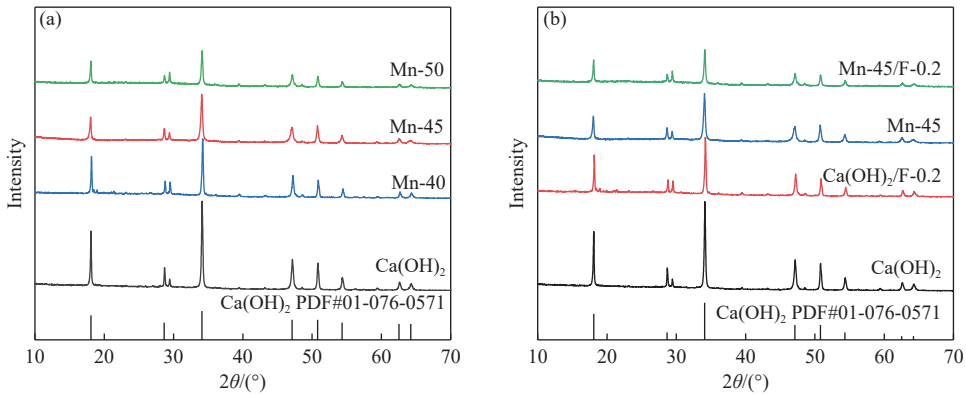


Fig. 1 (a) XRD patterns of $Ca(OH)_2$ and Mn-*x* adsorbents and (b) XRD patterns of $Ca(OH)_2$, $Ca(OH)_2$/F-0.2, Mn-45 and Mn-45/F-0.2 adsorbents

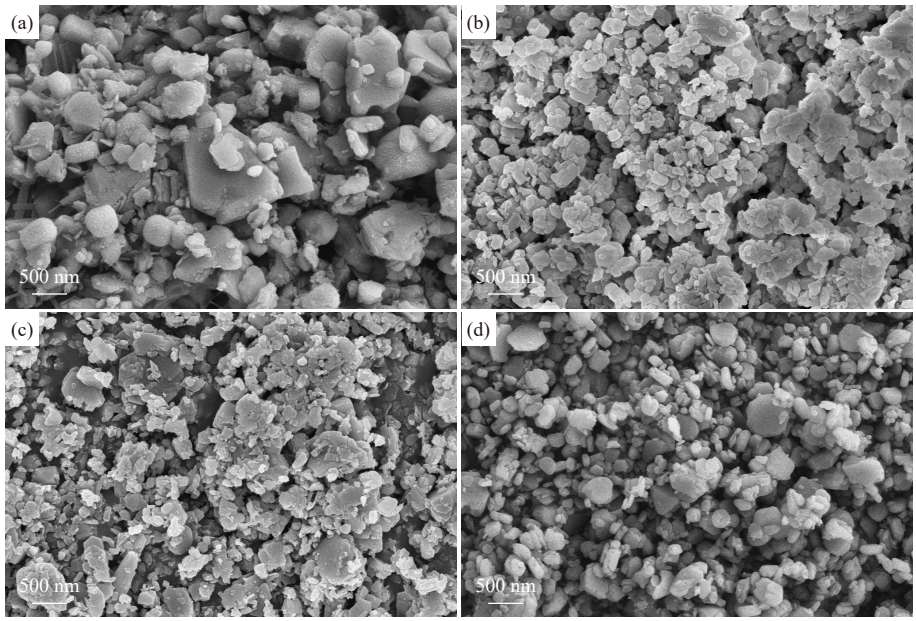


Fig. 2 SEM images of $Ca(OH)_2$ (a), $Ca(OH)_2$/F-0.2 (b), Mn-45 (c) and Mn-45/F-0.2 (d)

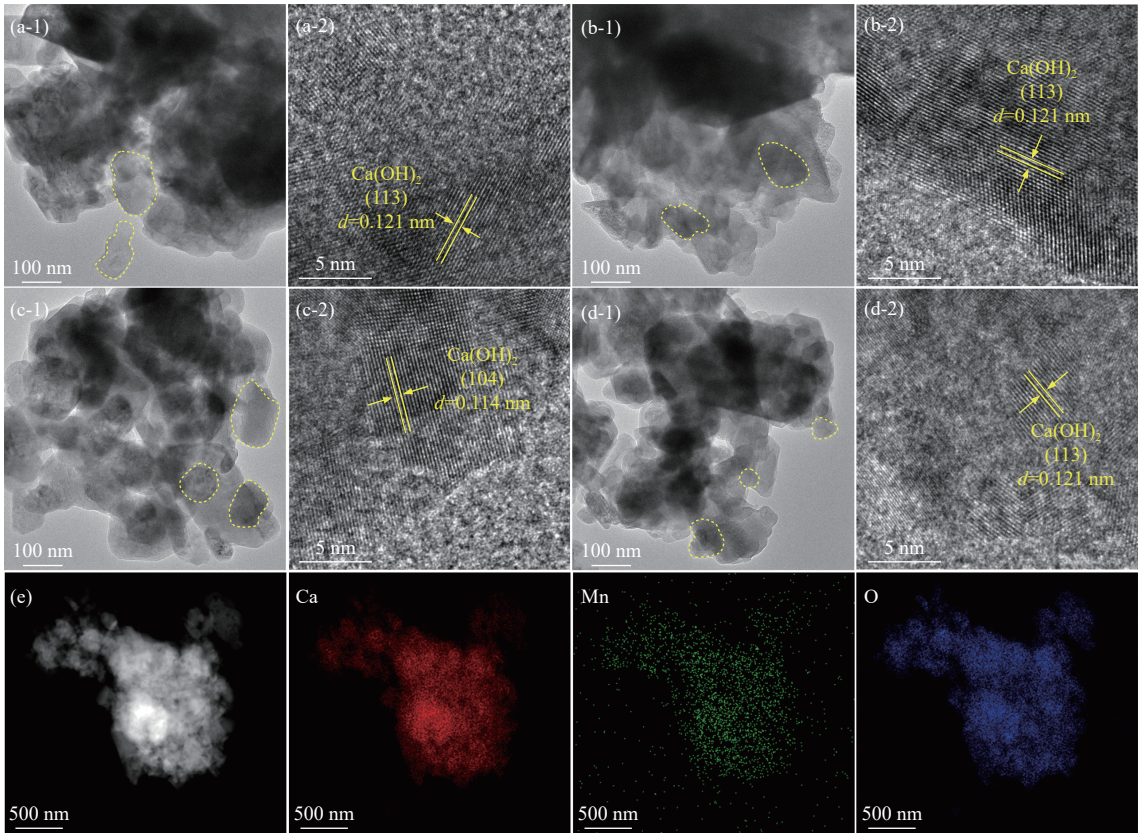


Fig. 3 TEM and HRTEM images of $Ca(OH)_2$ (a), $Ca(OH)_2$/F-0.2 (b), Mn-45 (c) and Mn-45/F-0.2 (d) and (e) element mapping of Mn-45/F-0.2 adsorbents

Figure 4(b) illustrates the pore size distribution of the adsorbent samples, further confirming their similar mesoporous structures. The physical properties of the adsorbent samples, including specific surface area, pore volume, and pore size, are summarized in Table 2. The comparison reveals that the $Ca(OH)_2$ and $Ca(OH)_2$/F-0.2 samples exhibit similar specific surface area, pore volume, and average pore diameter, indicating that F127 does not significantly enhance the physical structure of the Ca-based material. Compared to $Ca(OH)_2$ and $Ca(OH)_2$/F-0.2, the specific surface area of the Mn-45 and Mn-45/F-0.2 samples increased to approximately 23 from 18.6 m^2/g,

while the pore volume and average pore diameter increased to approximately 0.09 cm^3/g and 1.08 nm, respectively. This suggests that Mn doping favors to enlarge the specific surface area and optimize the pore structure of the adsorbent.

2.1.4 Surface chemical properties and defect structures of adsorbents

The chemical states of surface elements in the adsorbents were analyzed by XPS, and the results are presented in Figure 5(a)−(c). In the O 1*s* XPS spectra (Figure 5(a)), two characteristic peaks are observed at ~531.2 and 532.9 eV, corresponding to the O−H bonds in the hydroxyl lattice oxygen of $Ca(OH)_2$ and the adsorbed water molecules, respectively[19−20]. In contrast to $Ca(OH)_2$ and $Ca(OH)_2$/F-0.2, the feature of the hydroxyl lattice oxygen in the Mn-45 and Mn-45/F-0.2 samples shifts to the higher binding energy of 531.3 eV, suggesting the successful incorporation of Mn into the crystal lattice of $Ca(OH)_2$. Due to the stronger electronegativity of Mn atoms compared to the Ca atoms, the Mn–O bonds are stronger than the Ca–O bonds, and therefore depletes the electron density around the surrounding O atoms, resulting in an increase in binding energy. In the Ca 2*p* XPS spectra (Figure 5(b)), all Ca-based adsorbents display the typical doublet structure of Ca^{2+}, with characteristic peaks observed at approximately 346.8 and 350.4 eV, corresponding to the Ca $2p_{3/2}$ and Ca $2p_{1/2}$ orbitals, respectively[21−22]. Notably, compared to $Ca(OH)_2$ and $Ca(OH)_2$/F-0.2, the Ca 2*p* doublet peaks in the Mn-45 and Mn-45/F-0.2 samples shifted to a higher binding energy by approximately 0.1 eV. The increase in Ca 2*p* binding energy is primarily attributed to lattice distortion effects induced by Mn doping into the $Ca(OH)_2$ structure. Thus, it can be concluded that Mn doping substantially alters the chemical environment and electronic structure around the O and Ca atoms in the Ca-based adsorbent[22]. Figure 5(c) displays the Mn 2*p* XPS spectra of the Mn-45 and Mn-45/F-0.2 samples. Due to the low Mn content in the samples, the intensity of the Mn 2*p* XPS spectra is relatively low. However, XPS analysis revealed that the surface Mn concentrations of the Mn-45 and Mn-45/F-0.2 samples were 0.38% and 0.46%, respectively. This suggests that the introduction of the surfactant F127 enhances the distribution of Mn on the surface of the Ca-based adsorbent, thereby increasing the surface Mn concentration.

Furthermore, low-temperature ESR was used to examine the defect structures of the Ca-based adsorbents, with the results shown in Figure 5(d). The symmetric signal at g = 2.003 is ascribed to the unpaired electrons of oxygen vacancies (OVs) in the adsorbent, and the signal intensity corresponds to the concentration of OVs[23]. The OVs signal on various samples decreased by the order of Mn-45/F-0.2 > Mn-45 > $Ca(OH)_2$/F-0.2 > $Ca(OH)_2$. The low-temperature ESR results indicate that the surfactant F127 inhibits particle agglomeration in $Ca(OH)_2$, reduces its crystallinity, and thereby promotes the formation of oxygen vacancy structures. Mn doping results in partial incorporation of Mn atoms into the $Ca(OH)_2$ structure, inducing lattice distortion and thereby significantly increasing the concentration of OVs in the adsorbent. The synergistic effect of F127 and Mn doping further enhances the structural defects in $Ca(OH)_2$, resulting in the high concentration of OVs on the Mn-45/F-0.2 sample. It is widely accepted that the OVs serve as highly efficient active sites for the adsorption and subsequent activation of gaseous O_2 molecules into highly reactive chemisorbed oxygen species *via* electron transfer.

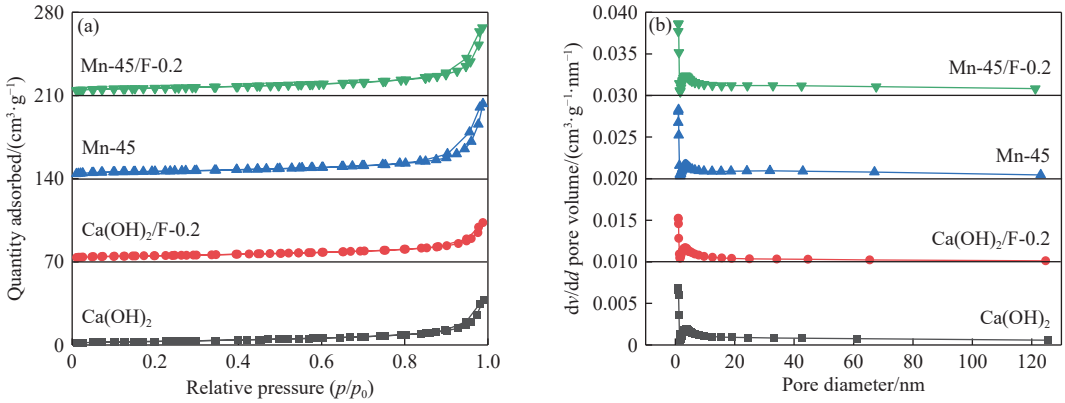


Fig. 4 N_2 adsorption-desorption curves (a) and pore size distribution curves (b) of the Ca-based adsorbents

Table 2 Physical properties of the as-prepared Ca-based adsorbent

Sample	BET surface area $S_{BET}/(m^2 \cdot g^{-1})$	Total pore volume $v/(cm^3 \cdot g^{-1})$	Average pore size d/nm
$Ca(OH)_2$	18.6	0.061	0.098
$Ca(OH)_2$/F-0.2	17.8	0.050	1.037
Mn-45	23.7	0.097	1.082
Mn-45/F-0.2	23.6	0.087	1.083

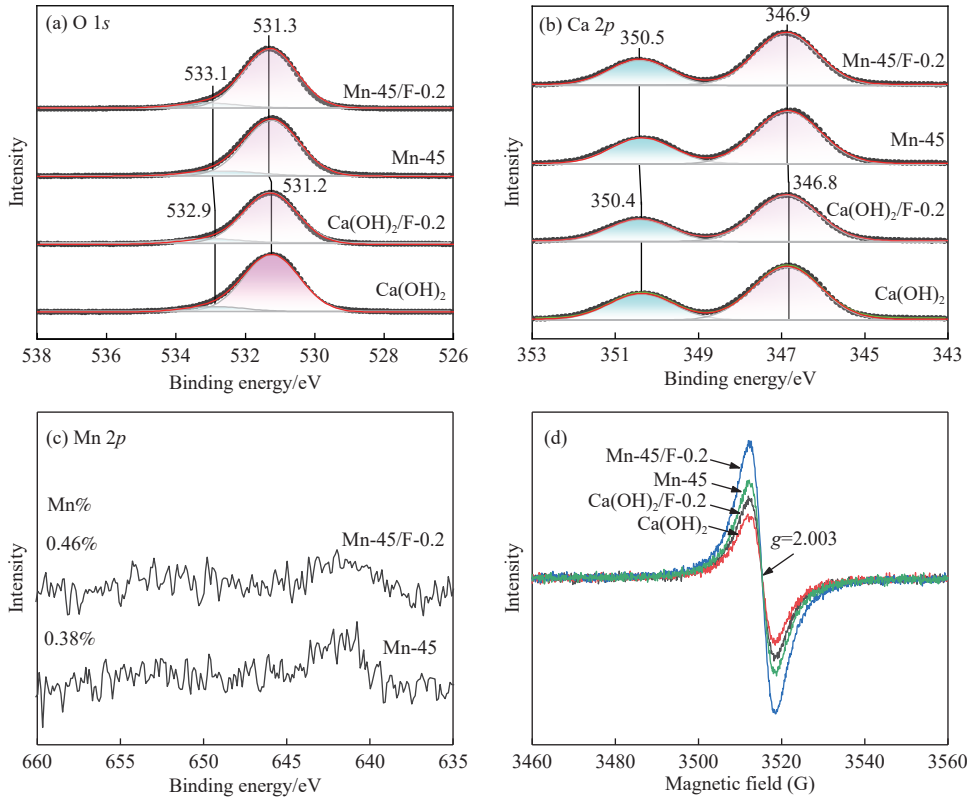


Fig. 5 XPS spectra of Ca-based adsorbents: (a) O 1*s*, (b) Ca 2*p* and (c) Mn 2*p* and (d) low-temperature ESR spectra

These species possess a superior oxidation capacity compared to lattice oxygen, thereby significantly accelerating the oxidation reaction rate[24–25]. During the desulfurization process, the active oxygen species rapidly oxidize adsorbed SO_2 to SO_3, which is more readily absorbed by $Ca(OH)_2$, thus facilitating the desulfurization reaction. Similarly, these active oxygen species can directly oxidize gaseous Hg^0 to Hg^{2+}, which is more easily captured, thereby enhancing the mercury removal performance of material.

2.2 Removal performance of SO_2 and Hg^0 by Ca-based adsorbents

2.2.1 SO_2 removal performance of adsorbents

The performance of Ca-based materials in the dry desulfurization reaction was measured. Figure 6(a) shows the effect of Mn doping on the desulfurization performance of materials. Moderate Mn doping was found to enhance the desulfurization performance of the Ca-based adsorbent. When 45 μL of $Mn(NO_3)_2$ solution was added, the Ca-based adsorbent exhibited optimal desulfurization performance. No significant improvement in desulfurization performance was observed with $Mn(NO_3)_2$ solution additions of 40 and 50 μL. The effect of the synergistic modification of Mn doping and F127 on the desulfurization performance of the samples is shown in Figure 6(b). The study found that when 45 μL of $Mn(NO_3)_2$ solution was added, an optimal F127 modification of 0.2 g further enhanced the SO_2 absorption reaction. Figure 6(c), (d) present the comparison of the SO_2 breakthrough curves and breakthrough sulfur capacities of the $Ca(OH)_2$, $Ca(OH)_2$/F-0.2, Mn-45 and Mn-45/F-0.2 adsorbents. As shown, the synergistic modification with F127 surfactant and Mn doping improved the desulfurization performance of the Ca-based adsorbent. Compared to the $Ca(OH)_2$ sample, the SO_2 breakthrough time was extended from 50.9 to 54.5 min, and the breakthrough sulfur capacity increased from 190.2 to 205.4 mg/g. This may be due to Mn doping, combined with appropriate F127 modification, optimizing the pore structure of the adsorbent. Simultaneously, it introduces Mn active sites that enhance the desulfurization performance of the Ca-based material by promoting SO_2 oxidation.

The effects of SO_2 concentration and flue gas temperature on the desulfurization performance of the optimized Mn-45/F-0.2 adsorbent have been systematically investigated, and the results are presented in Figure 7(a), (b). The study found that with the increase of SO_2 concentration from 2.0×10^{-4} to 6.0×10^{-4}, the SO_2 breakthrough time of the adsorbent decreased from 118.0 to 42.4 min. This is because high concentrations of SO_2 accelerate the coverage of active sites on the surface of adsorbent, leading to the rapid deposition of desulfurization products ($CaSO_3$/$CaSO_4$) within the pores. This leads to pore blockage and a sharp increase in internal diffusion resistance, ultimately inhibiting deeper SO_2 reactions. Within the temperature range of 300–375 °C, the reactivity of the adsorbent improved significantly by elevating the reaction temperature.

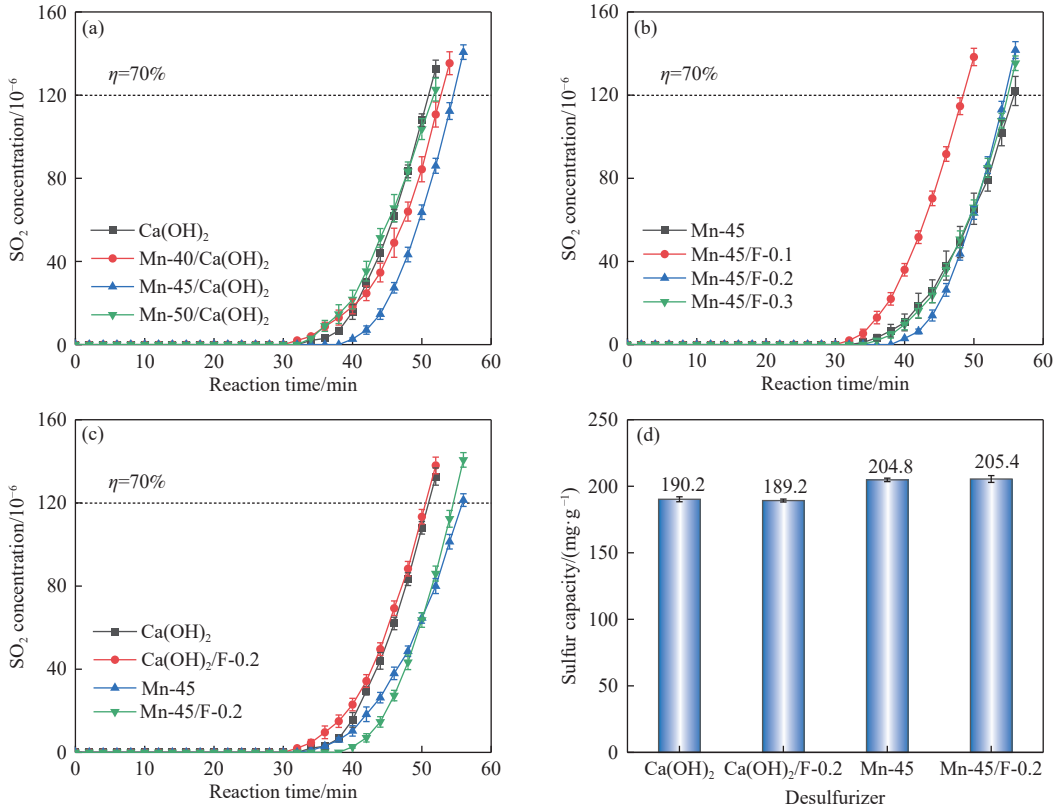


Fig. 6 (a) SO_2 breakthrough curves of $Ca(OH)_2$ and Mn-*x* adsorbents, (b) SO_2 breakthrough curves of Mn-45 and Mn-45/F-*y* adsorbents and (c), (d) $Ca(OH)_2$, $Ca(OH)_2$/F-0.2, Mn-45 and Mn-45/F-0.2 adsorbents
Reaction conditions: O_2 = 4%, gas flow = 1000 mL/min, GHSV = 26000 h^{-1}, desulfurization temperature = 350 °C.

When the reaction temperature was increased from 300 to 375 °C, the SO_2 breakthrough time was extended from 24.0 to 69.0 min. This is because the increase in reaction temperature accelerates the chemical reaction rate and enhances the diffusion rate of ions through the desulfurization product layer, thereby mitigating, to some extent, the blocking effect of the product layer on the reaction[26]. However, when the flue gas temperature was further increased to 400 °C, the reactivity of the adsorbent became similar to that at 375 °C. The reason for this is that at higher temperatures, the reaction rate between SO_2 and the Ca-based material becomes excessively rapid. The rapid formation of $CaSO_3$/$CaSO_4$ leads to increased diffusion resistance within the product layer, thereby limiting the further progression of the reaction[27].

In addition, the effects of flue gas humidity and NO concentration on the desulfurization performance of Mn-45/F-0.2 were investigated, with the results shown in Figure 7 (c), (d). The study found that a moderate level of flue gas humidity enhances the desulfurization reaction. The desulfurization efficiency of the Ca-based material was highest at a water vapor content of 20%, where the SO_2 breakthrough time increased from 50.9 min under dry flue gas conditions to 67.7 min. In contrast, at water vapor contents of 10% and 30%, the desulfurization efficiency of the Ca-based material was slightly lower than that under dry flue gas conditions. The reason is that under the appropriate humidity, a sufficiently thick liquid film forms on the surface of the adsorbent. This promotes the dissolution of SO_2 into HSO_3^- or SO_3^{2-}, which then diffuse through the liquid film to react with the adsorbent, forming $CaSO_3$/$CaSO_4$. In this process, water molecules act as a reaction medium, accelerating the reaction rate between ions and facilitating the desulfurization reaction[28]. However, when the flue gas humidity is too low, the adsorbent surface cannot form an effective liquid film, leading to pore blockage. Conversely, when the flue gas humidity is excessively high, the liquid film on the adsorbent surface thickens, increasing the resistance of gas-liquid mass transfer and causing the compaction of the adsorbent particles, which in turn results in the rapid SO_2 breakthrough. The NO component in the flue gas exerts an inhibitory effect on the desulfurization reaction. When the NO concentration increased from 0 to 6.0×10^{-4}, the SO_2 breakthrough time decreased from 50.9 to 45.3 min. This is because, in the presence of O_2, NO can be oxidized in the gas phase to form highly reactive NO_2, which then competes with SO_2 for the surface active sites on the adsorbent. Furthermore, as a highly reactive acidic substance, NO_2 preferentially reacts with the $Ca(OH)_2$ phase to form $Ca(NO_3)_2$, thereby covering the alkaline sites on the adsorbent surface and inhibiting the desulfurization reaction[29].

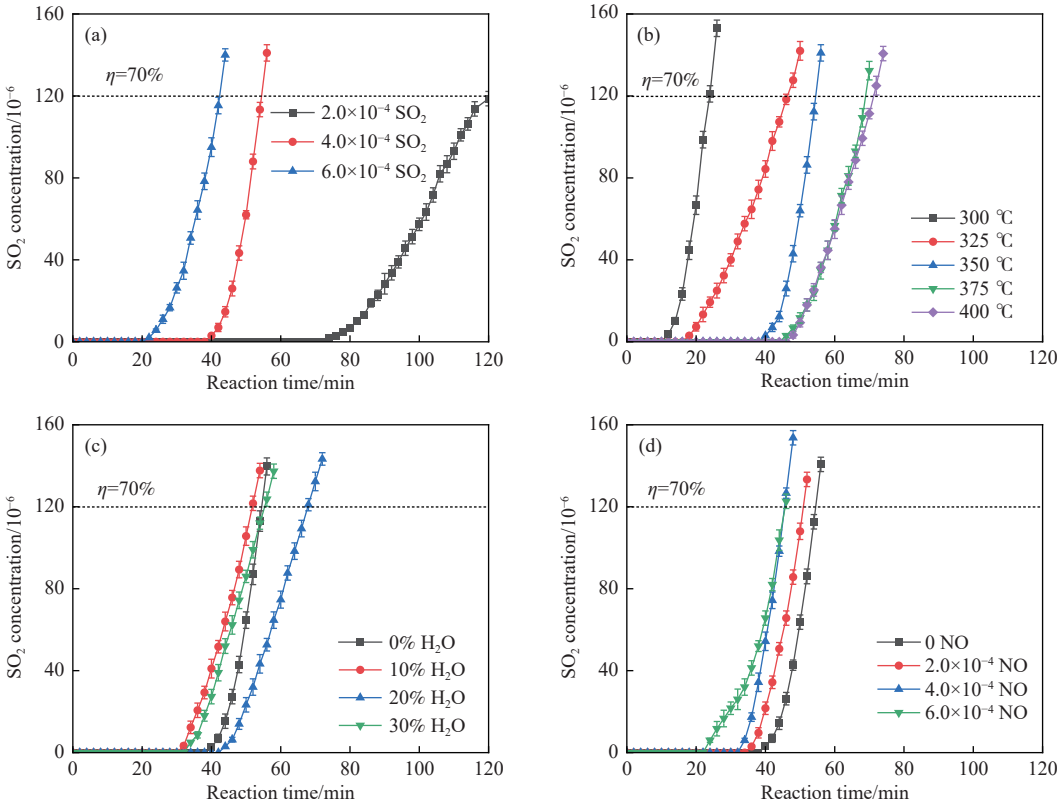


Fig. 7 Influence of flue gas conditions on desulfurization efficiency of Mn-45/F-0.2 sample: (a) SO_2 concentration, (b) reaction temperature, (c) water vapor content, and (d) NO concentration
Reaction conditions: $SO_2 = 4.0\times10^{-4}$ (except Figure 7(a)), $O_2 = 4\%$, flue gas flow = 1000 mL/min, GHSV == 26000 h^{-1}, desulfurization temperature = 350 °C (except Figure 7(b)).

Furthermore, to investigate the utilization rate of Mn-45/F-0.2 in dry desulfurization reactions, cyclic desulfurization performance tests were conducted, with the results presented in Figure 8. The study found that when the Mn-45/F-0.2 sample was applied in the second desulfurization reaction, the SO_2 breakthrough time was significantly reduced, decreasing from 54.5 min in the first reaction to 4.0 min.

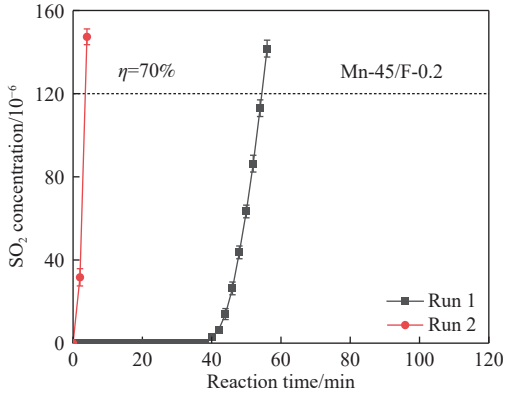


Fig. 8 Mn-45/F-0.2 regeneration cycle desulfurization breakthrough curves
Reaction conditions: $SO_2 = 4.0\times10^{-4}$, $O_2 = 4\%$, gas flow = 1000 mL/min, GHSV = 26000 h^{-1}, desulfurization temperature = 350 °C.

This indicates that the Ca-based absorption sites in Mn-45/F-0.2 were nearly fully consumed during the initial desulfurization cycle. This characteristic is advantageous for reducing the Ca/S ratio in practical dry desulfurization applications, thereby reducing operational costs.

2.2.2 Hg^0 removal performance of adsorbents

The Hg^0 removal performance of the $Ca(OH)_2$, $Ca(OH)_2$/F-0.2, Mn-45 and Mn-45/F-0.2 samples was investigated. As shown in Figure 9(a), the Hg^0 removal efficiencies for the $Ca(OH)_2$, $Ca(OH)_2$/F-0.2, Mn-45 and Mn-45/F-0.2 samples were 10.4%, 11.2%, 13.7% and 14.9%, respectively. These results emphasize the considerable potential of Ca-based adsorbents in the Hg^0 removal and simultaneously demonstrate that synergistic modifications, including surfactant protection and Mn doping, enhance the Hg^0 removal performance of the Ca-based material. The mechanism for the promoted performance of Mn-45/F-0.2 in the Hg^0 removal reaction is hypothesized as follow: Mn species acting as the catalytic sites, promoting Hg^0 oxidation through their redox cycles (e.g., Mn^{3+}/Mn^{4+})[30]; Mn doping inducing the formation of OVs in the Ca-based material, which facilitates the adsorption and activation of O_2 molecules, thereby accelerating Hg^0 oxidation[31]; and the synergistic

modification through Mn doping and F127 addition, increasing the specific surface area and pore volume of the Ca-based adsorbent, thereby providing the efficient mass transfer channels for Hg^0 diffusion. Concurrently, F127 enhances the dispersion of Mn sites, thereby improving the utilization efficiency of Mn catalytic sites and facilitating the effective contact between Hg^0 and the active sites.

For the Mn-45/F-0.2 material, the effects of SO_2 concentration, NO concentration, and the co-presence of SO_2/NO on the Hg^0 removal performance were investigated. As shown in Figure 9(b), (c), the acidic flue gas components SO_2 and NO exhibit distinctly different effects on Hg^0 removal. As the SO_2 concentration increased from 0 to 5.0×10^{-4}, the Hg^0 removal efficiency decreased from 14.9% to 8.6%. In contrast, as the NO concentration increased from 0 to 6.0×10^{-4}, the Hg^0 removal efficiency increased from 14.9% to 22.5%. The inhibition of Hg^0 removal by SO_2 primarily arises from two aspects: SO_2 competes with Hg^0 for surface-active sites and can cause sulfation of the Mn sites, thereby blocking the catalytic oxidation of Hg^0 at these sites[32], and the desulfurization products ($CaSO_3$/$CaSO_4$) readily clog the pores of the calcium-based material, inhibiting both the adsorption and oxidative removal of Hg^0. In contrast, the promotion of Hg^0 removal by NO is attributed to the abundant OVs in the Mn-45/F-0.2 sample, which can generate surface-adsorbed oxygen species. NO is oxidized to NO_2 under the synergistic action of these surface-adsorbed oxygen species and the Mn catalytic sites. As a strong oxidant, NO_2 then oxidizes Hg^0 to Hg^{2+}, thereby enhancing the Hg^0 removal efficiency[33−34]. Figure 9(d) compares the Hg^0 removal performance of the Mn-45/F-0.2 material under conditions of SO_2 alone, NO alone, and the co-presence of SO_2/NO. The study found that in flue gas environments where SO_2 and NO coexist, the inhibitory effect of SO_2 on Hg^0 removal can be significantly mitigated. When both SO_2 and NO concentrations were 4.0×10^{-4}, the Hg^0 removal efficiency of the Mn-45/F-0.2 material reached 15.5%, demonstrating its potential applicability for the cooperative control of SO_2 and Hg^0 in biomass boiler flue gas. However, compared to highly efficient Mn-based Hg^0 removal catalysts, the Hg^0 removal performance of the Mn-45/F-0.2 adsorbent remains relatively low. This is primarily attributed to the fact that its material design is still fundamentally oriented towards desulfurization. The main component, $Ca(OH)_2$, is a typical alkali absorbent that lacks favorable redox properties, making it difficult to provide an effective reaction environment required for the highly efficient catalytic oxidation of Hg^0. In follow-up research, introducing typical catalyst support materials for Hg^0 oxidation (such as TiO_2, Al_2O_3, etc.) to modify the Ca-based adsorbent through composite design could be considered. This would help create a more suitable catalytic microenvironment for the Mn species, thereby enhancing their promotional effect in the catalytic oxidation of Hg^0.

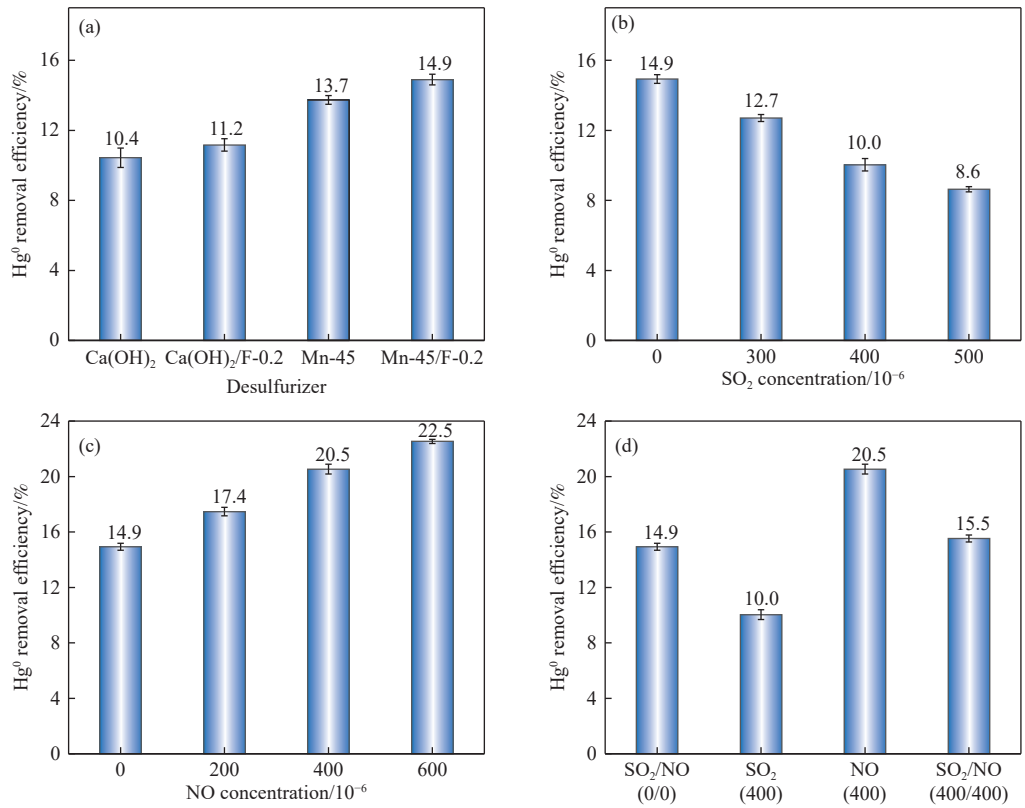


Fig. 9 (a) Hg^0 removal performance of $Ca(OH)_2$, $Ca(OH)_2$/F-0.2, Mn-45 and Mn-45/F-0.2 samples, (b) effect of SO_2 concentration on the Hg^0 removal performance of Mn-45/F-0.2, (c) effect of NO concentration on Hg^0 removal performance of Mn-45/F-0.2 and (d) effects of SO_2 and NO components on Hg^0 removal performance of Mn-45/F-0.2

2.3 Reaction mechanism of SO_2/Hg^0 synergistic control by the Ca-Mn composite adsorbent

To investigate the synergistic removal mechanism of SO_2/Hg^0 by Ca-based materials, XRD characterization was conducted on the $Ca(OH)_2$/F-0.2 and Mn-45/F-0.2 samples before and after reaction. Figure 10(a) compares the XRD patterns of the $Ca(OH)_2$/F-0.2 and Mn-45/F-0.2 samples after SO_2 breakthrough in the desulfurization reaction. It can be observed that after SO_2 breakthrough, the composition of both the $Ca(OH)_2$/F-0.2 and Mn-45/F-0.2 samples transformed from $Ca(OH)_2$ into the desulfurization products $CaSO_3/CaSO_4$ and the dehydration product CaO. Notably, the diffraction peak intensity of CaO on the Mn-45/F-0.2 sample is slightly lower than that on the $Ca(OH)_2$/F-0.2 sample, indicating that Mn doping modification improved the utilization rate of the $Ca(OH)_2$ component during the desulfurization reaction. Figure 10(b) displays the XRD patterns of the Ca-based materials after 12 h of the desulfurization reaction. Compared to $Ca(OH)_2$/F-0.2, the diffraction peaks for $CaSO_3$, $CaSO_4$ and CaO on the Mn-45/F-0.2 sample are stronger and sharper. This suggests that the Mn doping, which optimized the physical structure (specific surface area and pore structure) of adsorbent and accelerated SO_2 oxidation, significantly promoted the absorption of SO_2/SO_3 by $Ca(OH)_2$. Meanwhile, the dense $CaSO_3/CaSO_4$ product layer hindered the mass transfer, limiting the further reaction between SO_2 and the deeper Ca-based species. Under the catalysis of Mn sites, $Ca(OH)_2$ was more readily and thoroughly converted into crystalline CaO, which accounts for the significant enhancement of the characteristic CaO diffraction peaks. Figure 10(c) presents the XRD patterns of the Ca-based materials after 12 h of Hg^0 removal reaction. Both the $Ca(OH)_2$/F-0.2 and Mn-45/F-0.2 samples primarily consist of CaO species. However, $Ca(OH)_2$ characteristic peaks of certain intensity were detected on the $Ca(OH)_2$/F-0.2 sample, indicating that the presence of Mn sites promoted the dehydration of $Ca(OH)_2$ under high-temperature conditions. Due to the low concentration of Hg^0 in the flue gas, no characteristic peaks of Hg-containing species were detected on the surface of either sample. Figure 10(d) shows the XRD patterns of the Ca-based materials after 12 h of simultaneous SO_2/Hg^0 removal reaction. The results are similar to those in Figure 10 (b), suggesting that the co-presence of SO_2 and Hg^0 did not significantly affect the progression of the desulfurization reaction or the composition of the desulfurization products.

The XPS results for the $Ca(OH)_2$/F-0.2 and Mn-45/F-0.2 samples following the reaction are presented in Figure 11. Figure 11(a) presents the S 2*p* XPS spectra of the samples following SO_2 breakthrough in the desulfurization reaction. In the spectra, the characteristic peaks at 167.1 and 168.4 eV are attributed to the S $2p_{3/2}$ and S $2p_{1/2}$ orbitals of SO_3^{2-} species, while the peaks at 169.1 and 170.3 eV correspond to the S $2p_{3/2}$ and S $2p_{1/2}$ orbitals of SO_4^{2-} species[35−36].

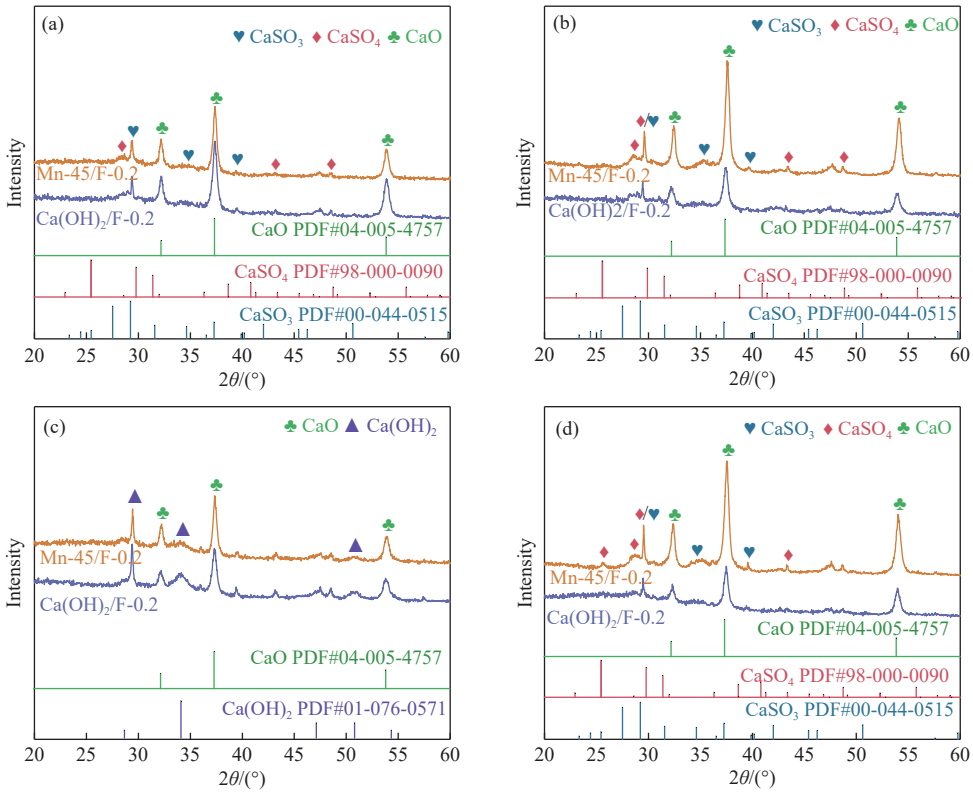


Fig. 10 XRD patterns of $Ca(OH)_2$/F-0.2 and Mn-45/F-0.2 after reactions: (a) desulfurization reaction after breakthrough, (b) desulfurization reaction for 12 h, (c) Hg^0 removal reaction for 12 h and (d) synergistic removal of SO_2/Hg^0 for 12 h

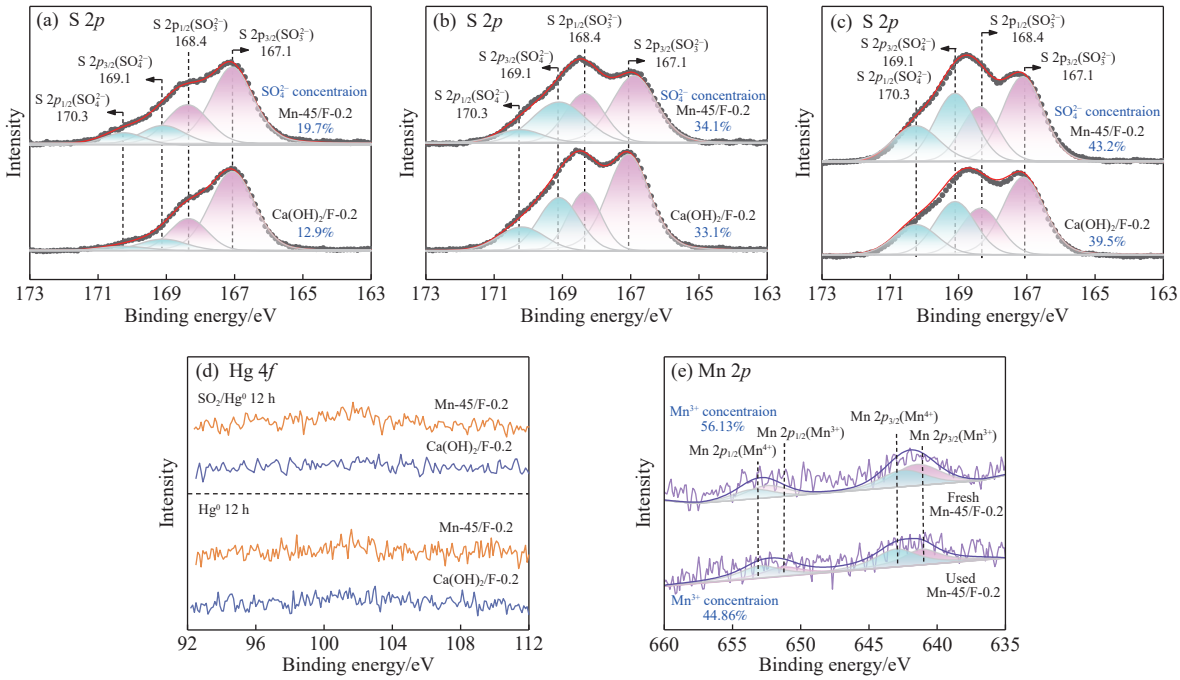


Fig. 11 XPS spectra of $Ca(OH)_2$/F-0.2 and Mn-45/F-0.2 after reactions: (a) S 2*p* XPS spectra of samples from the desulfurization reaction after breakthrough, (b) S 2*p* XPS spectra of samples from desulfurization reaction for 12 h, (c) S 2*p* XPS spectra of samples from synergistic removal of SO_2/Hg^0 for 12 h, (d) Hg 4*f* XPS spectra of samples from synergistic removal of SO_2/Hg^0 for 12 h, and (e) Mn 2*p* XPS spectra of the Mn-45/F-0.2 sample before and after the synergistic removal of SO_2/Hg^0

Calculations based on the characteristic peak areas indicate that after SO_2 breakthrough, the surface concentration of SO_4^{2-} on the Mn-45/F-0.2 sample (19.7%) was significantly higher than that on the $Ca(OH)_2$/F-0.2 sample (12.9%). This suggests that Mn modification effectively promoted the oxidation of SO_2 to SO_3, thereby facilitating the absorption of SO_2 by the Ca-based material, enhancing its desulfurization efficiency, and increasing the accumulation of surface sulfate products. As shown in Figure 11(b), the S 2*p* XPS spectra of the samples after 12 h of the desulfurization reaction are presented. Compared to Figure 11(a), the surface concentration of SO_4^{2-} on both samples increased significantly to approximately 34%. This phenomenon suggests that with the extension of the desulfurization reaction time, the sulfite products formed on the surface of the adsorbent are gradually oxidized and converted into sulfate products. Combined with the results from Figure 11(a), the primary role of Mn modification lies in promoting the initial oxidation stage of SO_2 to SO_3, while its catalytic effect on the subsequent oxidation reaction from sulfite to sulfate is not significant. Figure 11(c) presents the S 2*p* XPS spectra of the samples after 12 h of simultaneous desulfurization and Hg^0 removal. The spectra are similar to those in Figure 11(b), suggesting that the presence of Hg^0 did not significantly affect the desulfurization reaction process or the composition of products on the adsorbent surface. Figure 11(d) presents the Hg 4*f* XPS spectra of the samples after 12 h of Hg^0 removal and after 12 h of simultaneous SO_2/Hg^0 removal. However, due to the low concentration of mercury species on the sample surfaces, the obtained XPS signals are weak.

Additionally, the Mn 2*p* XPS spectra of the Mn-45/F-0.2 sample were compared before and after 12 h of simultaneous SO_2/Hg^0 removal. As depicted in Figure 11(e), a following the reaction, the Mn 2*p* characteristic peaks shifted to higher binding energy, suggesting a decrease in electron cloud density around the Mn atoms and an increase in the oxidation state of Mn. Peak deconvolution of the high-resolution Mn 2*p* spectra revealed that the molar percentages of surface Mn^{3+} and Mn^{4+} species in the fresh sample were 56.1% and 43.9%, respectively. After the reaction, the percentage of Mn^{3+} decreased to 44.8%, while that of Mn^{4+} increased to 55.2%. In catalytic oxidation reactions, Mn^{4+} species in Mn-based catalysts are generally regarded as highly active catalytic sites, while a suitable proportion of Mn^{3+} species also facilitates the oxidation process. This is because the concentration of OVs is positively correlated with the Mn^{3+} content. Furthermore, the Mn^{3+}–O bond is relatively longer and weaker, facilitating oxygen atom dissociation and allowing lattice oxygen to effectively participate in oxidation reactions[37−39]. Therefore, the decrease in the proportion of Mn^{3+} observed in Figure 11(e) after the reaction suggests that Mn^{3+}, Mn^{4+} and OVs collectively acted as catalytic sites in the oxidation reactions of SO_2 and Hg^0. Additionally, the redox cycle between Mn^{3+} and Mn^{4+} ensures the continuous progression of the catalytic oxidation reactions.

Based on the experimental results, the mechanism of dry desulfurization and synergistic Hg^0 control by the developed Ca-Mn composite adsorbent, Mn-45/F-0.2, is illustrated in Figure 12. During the preparation of the adsorbent, the introduction of the surfactant F127

effectively prevented the agglomeration of $Ca(OH)_2$ particles and promoted the uniform distribution of Mn within the calcium-based material. Mn doping resulted in the incorporation of partial Mn atoms into the $Ca(OH)_2$ crystal lattice, which not only suppressed the crystalline growth of $Ca(OH)_2$ but also optimized the pore structure of the adsorbent. This process enhanced the lattice distortion and induced the formation of abundant OVs. The Mn sites and adjacent OVs collectively form the active centers, which significantly enhance the oxidative capacity of the adsorbent. This promotes the rapid oxidation of SO_2 to SO_3, enabling its efficient absorption by the $Ca(OH)_2$ component, while simultaneously catalyzing the oxidation of Hg^0 to Hg^{2+} species, thus achieving the synergistic removal of SO_2/Hg^0. Additionally, the relatively large specific surface area and pore volume of Mn-45/F-0.2 significantly enhance the mass transfer of both SO_2 and Hg^0 to the active sites. This not only facilitates their contact with the active centers but also effectively mitigates the blockage of the pore structure by desulfurization products during the reaction. As a result, this leads to an extended SO_2 breakthrough time and enhanced Hg^0 removal efficiency.

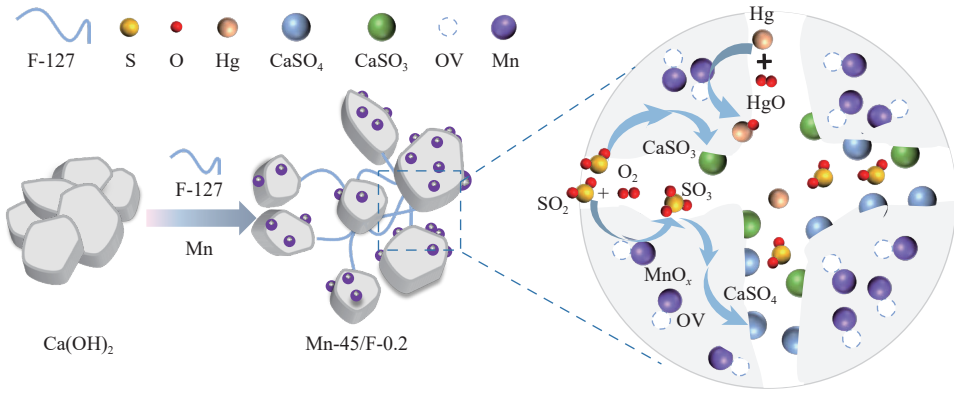


Fig. 12 Proposed mechanism for the synergetic removal of SO_2 and Hg^0 on the Mn-45/F-0.2 adsorbent

3 Conclusions

This study successfully developed a highly active Ca-Mn composite adsorbent, Mn-45/F-0.2, utilizing a synergistic modification strategy involving optimized dispersion with the F127 surfactant and enhanced oxidation through Mn doping. The material was subsequently employed in synergistic dry desulfurization and Hg^0 removal. The results indicated that, compared with unmodified $Ca(OH)_2$, the Mn-45/F-0.2 material exhibited an extended SO_2 breakthrough time from 50.9 to 54.5 min, an increased sulfur breakthrough capacity from 190.2 to 205.4 mg/g, and an improved Hg^0 co-removal efficiency from 10.4% to 14.9%. Characterization results revealed that Mn doping significantly suppressed the rapid crystallization and agglomeration of $Ca(OH)_2$ particles, enhanced the defect structure of the adsorbent, and simultaneously optimized its pore architecture, resulting in an increase in specific surface area and pore volume. F127 modification, in contrast, facilitated the uniform distribution of Mn in the Ca-based matrix and increased the surface concentration of Mn active sites. In the SO_2/Hg^0 synergistic removal reaction, Mn sites along with adjacent OVs, form the active centers that significantly enhance the oxidative capability of the adsorbent. This promotes the rapid oxidation of SO_2 to SO_3, which could be efficiently captured by the $Ca(OH)_2$ component, and simultaneously catalyzing the oxidation of Hg^0 to Hg^{2+} species. Moreover, the relatively large specific surface area and pore volume of Mn-45/F-0.2 enhance reaction mass transfer, accelerating the absorption of SO_2/SO_3 by the Ca-based material. This also effectively reduces pore blockage by desulfurization products, thereby extending the SO_2 breakthrough time and enhancing Hg^0 removal efficiency. This study provides experimental data and theoretical support for the modification technology of dry calcium-based adsorbents using the Ca-Mn composite adsorbent, offering valuable guidance for achieving efficient and cost-effective removal of low-concentration SO_2/Hg^0.

Declaration of Competing Interest

The authors declare no conflict of interest.

References

[1] TAN Z, NIU G, WANG Y, et al. Analysis of technical route for ultra-low emission of air pollutants in biomass direct-fired power plants[J]. Therm Power Gen, 2021, 50(10): 101−107.

[2] CAO W, LIU Q, YUAN Y, et al. Difficulties and optimum method of denitration for a biomass boiler[J]. Environ Eng, 2023, 41(S2): 299−301.

[3] ROKNI E, REN X, PANAHI A, et al. Emissions of SO_2, NO_x, CO_2, and HCl from Co-firing of coals with raw and torrefied biomass fuels[J]. Fuel, 2018, 211: 363−374.

[4] CHENG T, ZHOU X, YANG L, et al. Emission characteristics of soluble ions in fine particulates in limestone–gypsum wet flue gas desulfurization system[J]. Energy Fuels, 2020, 34(3): 3836−3842.

[5] YIN J, PENG B, GU Z, et al. Research progress on modification of dry calcium-based desulfurizers[J]. Clean

Coal Technol, 2024, 30(S1): 46−51.

[6] FAN X, WANG H, JIN Y, et al. Understanding the pore size distribution of $Ca(OH)_2$ for effective desulfurization under low-to-medium temperatures[J]. Powder Technol, 2024, 438: 119586.

[7] LI C, ZHANG T, LI J, et al. Research progress on mechanism and kinetics of SO_2 removal by dry desulfurizer[J]. Appl Chem Ind, 2015, 44(5): 927−932.

[8] WANG P, SHI M, ZHAO B, et al. $Ca(OH)_2$ nanosheets fabricated by carbide residue for effective dry desulfurization [J]. J Environ Chem Eng, 2025, 13: 116964.

[9] XING G, LI S, WANG Y, et al. From laboratory to industry: Preparation and mechanism analysis of organic additive-modified high-activity calcium hydroxide desulfurizer in low-temperature dry desulfurization [J]. Sep Purif Technol, 2025, 370: 133262.

[10] FAN X, WANG H, JIN Y, et al. On the synergistic modulation of $Ca(OH)_2$ microstructure for effective desulfurization by sodium dodecyl sulfate (SDS) mixed systems[J]. Fuel, 2025, 384: 134001.

[11] YU Q, REN Z, LIU S, et al. Construction of calcium-based materials with high specific surface area for dry desulfurization[J]. Coal Conver, 2025, 48(4): 166−176.

[12] ZHONG D, SUN Y, QU X, et al. Research and application of new efficient catalytic desulfurizer[J]. Inorg Salt Ind, 2022, 54(1): 109−111.

[13] YAO L, XIN G, PU P, et al. Promotion of manganese extraction and flue gas desulfurization with manganese ore by iron in the anodic solution of electrolytic manganese[J]. Hydrometallurgy, 2021, 199: 105542.

[14] WANG C. Study on performance and mechanism of high-efficiency calcium-based desulfurizer suitable for low-concentration SO_2 removal[D]. Jinan: Shandong University, 2023.

[15] FANG P, TANG Z, HUANG J, et al. Emission characteristics of flue gas pollutants emitted from biomass boilers and its control strategies[J]. Environ Sci Technol, 2016, 39(10): 155−160.

[16] YUAN B, MAO X, WANG Z, et al. Radical-induced oxidation removal of multi-air-pollutant: A critical review[J]. J Hazard Mater, 2020, 383: 121162.

[17] LI Y, CHEN M, XUE Z, et al. Research on synergistic mercury removal of coal-fired power plants[J]. Chem Ind Eng Progress, 2014, 33(8): 2187−2191.

[18] ZHOU X, WU Y, MI T, et al. Interaction mechanism between heavy metals and Ce-doped CaO in flue gas of coal combustion [J]. J Fuel Chem Technol, 2020, 48(12): 1520-1529.

[19] DENG J, WU F, GAO S, et al. Self-activated $Ni(OH)_2$ cathode for complete electrochemical reduction of trichloroethylene to ethane in low-conductivity groundwater [J]. Appl Catal B: Environ, 2022, 309: 121258.

[20] LIU Z, REN Z, WANG L, et al. Solidification/stabilization mechanism of compound heavy metal cations by phosphogypsum slag composite[J]. Sci China Technol Sci, 2025, 68(7): 1720501.

[21] XING G, LI S, WANG Y, et al. Experimental study on the preparation of desulfurizer for low temperature dry desulfurization by digesting CaO in urea solution[J]. J Environ Chem Eng, 2024, (12): 113865.

[22] XING G, ZHAO S, LI X, Mechanism and experimental study of desulfurizing agent based on Mn/Ce-Ca for sintering flue gas desulfurization (FGD) [J]. J Environ Chem Eng, 2023, 11: 111242.

[23] HONG W, ZHU T, LIU Y, et al. Rational co-introduction of K-Ce ions into OMS-2 tunnels to promote oxygen vacancies and Brönsted acid sites for enhanced NH_3-SCO[J]. Appl Catal B: Environ, 2025, 372: 125212.

[24] SHANG H, WANG X, LI H, et al. Oxygen vacancies promote sulfur species accumulation on TiO_2 mineral particles[J]. Appl Catal B: Environ, 2021, 290: 120024.

[25] LI B, HOU Y, GAO J, et al. Rational amelioration of redox equilibrium by constructing hollow nanotube Co-Mn/TiO_2 catalyst to boost simultaneous removal of NO and Hg^0[J]. Appl Catal B: Environ, 2024, 341: 123353.

[26] LIU P, YANG S, HU J, et al. Numerical analysis of SO_2 removal characteristics in industrial flue gas desulfurization reactor by spray drying adsorption[J]. Sep Purif Technol, 2023, 323: 124475.

[27] SHANG J. Study on layer diffusion mechanism of sulfurization products of calcium-based desulfurizer[D]. Baoding: North China Electric Power University, 2010.

[28] ZHOU Y, ZHU X, PENG J, et al. The effect of hydrogen peroxide solution on SO_2 removal in the semidry flue gas desulfurization process[J]. J Hazard Mater, 2009, 170: 436−442.

[29] LI Y, LIU Y, LI C, et al. Preparation of calcium-based composite absorbent and simultaneous removal performance of SO_x and NO_x from flue gas[J]. Chin J Process Eng, 2023, 23(10): 1446−1457.

[30] MA Y, MU B, ZHANG X, et al. Graphene enhanced Mn-Ce binary metal oxides for catalytic oxidation and adsorption of elemental mercury from coal-fired flue gas[J]. Chem Eng J, 2019, 358: 1499−1506.

[31] WANG S, YE D, LIU X, et al. Mn-Cr mixed oxide adsorbents with high SO_2 resistance for elemental mercury removal from coal-fired flue gas[J]. J Ind Eng Chem, 2023, 123: 260−271.

[32] XIAO Y, YANG Y, LIU J, et al. Effect mechanism of SO_2 on Hg^0 adsorption over $CuMn_2O_4$ sorbent[J]. Fuel, 2022, 329: 125399.

[33] YANG Z, YAO Q, ZHU J, et al. Co-doped $CeMnO_3$ perovskite for NO catalytic oxidation and co-benefit of elemental mercury removal from oxy-fuel combustion flue gas[J]. Chem Eng J, 2025, 514: 163335.

[34] MA A, ZHAO S, LUO H, et al. Effects of coal-fired flue gas components on mercury removal by the mechanochemical s-modified petroleum coke[J]. ACS Omega, 2022, 7(35): 31205−31217.

[35] HAO R, WANG X, ZHAO X, et al. A novel integrated method of vapor oxidation with dual absorption for simultaneous removal of SO_2 and NO[J]. Chem Eng J, 2018, 333: 583−593.

[36] LI Y, LIN Y, XU Z, et al. Oxidation mechanisms of H_2S by oxygen and oxygen-containing functional groups on activated carbon[J]. Fuel Process Technol, 2019, 189:

110−119.

[37] YANG W, SU Z, XU Z, et al. Comparative study of α-, β-, γ- and δ-MnO_2 on toluene oxidation: Oxygen vacancies and reaction intermediates[J]. Appl Catal B: Environ, 2020, 260: 118150.

[38] WANG Q, WANG Y, WEI L, et al. Promotional mechanism of activity of CeEuMnO_x ternary oxide for low temperature SCR of NO_x[J]. J Rare Earth, 2023, 41: 965−974.

[39] MO S, ZHANG Q, LI J, et al. Highly efficient mesoporous MnO_2 catalysts for the total toluene oxidation: Oxygen-vacancy defect engineering and involved intermediates using in situ DRIFTS[J]. Appl Catal B: Environ, 2020, 264: 118464.

钙锰复合脱硫剂构筑及其 SO_2/Hg^0 协同脱除研究

刘帅鹏[1,2]，李大来[1,2]，任子晗[1,2]，刘　洁[1,2,*]，汪黎东[1,2]

（1. 华北电力大学燕赵电力实验室, 河北 保定 071003; 2. 华北电力大学环境科学与工程系, 河北 保定 071003）

摘　要: 碳中和战略下, 生物质锅炉成为可再生能源利用的关键设施。针对生物质锅炉烟气低浓度 SO_2 排放特征, 钙基干法脱硫技术具有结构紧凑、基建投资少、运维简便等优势, 但普遍存在脱硫剂利用率低及脱硫效率不高的瓶颈问题。本研究开发了一种基于 F127 表面活性剂优化分散和 Mn 元素掺杂氧化增效协同策略的新型 Ca-Mn 复合脱硫剂。Mn 元素与 F127 的引入有效抑制了 $Ca(OH)_2$ 晶粒团聚, 优化了脱硫剂的孔隙结构, 同时诱导了丰富氧空位结构。改性脱硫剂较大的比表面积和孔容促进了反应传质, 并有效防止了脱硫产物堵塞孔隙结构、覆盖反应位点; Mn 位点和氧空位构成催化中心, 不仅通过促进 SO_2 氧化加速脱硫反应进行, 同时使脱硫剂耦合 Hg^0 催化氧化功能, 实现了 SO_2/Hg^0 的高效协同脱除。

关键词: 钙锰复合材料; 氧空位; 干法脱硫; 零价汞; 协同控制

中图分类号: X511　　**文献标识码:** A

作者简介:



刘帅鹏(2000), 硕士, 研究方向为烟气污染物控制, 15694888795@163.com。



刘洁(1986), 博士, 教授, 研究方向为烟气污染物控制及资源化利用, jie.liu@ncepu.edu.cn。